



Cite this: DOI: 10.1039/c6sm01281g

# Blast wave attenuation in liquid foams: role of gas and evidence of an optimal bubble size

Martin Monloubou, Myrthe A. Bruning, Arnaud Saint-Jalmes, Benjamin Dollet and Isabelle Cantat\*

Received 3rd June 2016,  
Accepted 19th August 2016

DOI: 10.1039/c6sm01281g

www.rsc.org/softmatter

Liquid foams are excellent systems to mitigate pressure waves such as acoustic or blast waves. The understanding of the underlying dissipation mechanisms however still remains an active matter of debate. In this paper, we investigate the attenuation of a weak blast wave by a liquid foam. The wave is produced with a shock tube and impacts a foam, with a cylindrical geometry. We measure the wave attenuation and velocity in the foam as a function of bubble size, liquid fraction, and the nature of the gas. We show that the attenuation depends on the nature of the gas and we experimentally evidence a maximum of dissipation for a given bubble size. All features are qualitatively captured by a model based on thermal dissipation in the gas.

## 1 Introduction

Pressure wave propagation in liquid foams is very peculiar, with a low sound velocity, of the order of  $50 \text{ m s}^{-1}$ , and a high level of attenuation. This feature is of high interest in the context of soundproofing or of blast wave attenuation.<sup>1–7</sup> Recent progress has been made in the identification of the local processes controlling the propagation velocity and the attenuation length. In his seminal work, Wood<sup>8</sup> described the foam as an effective continuum, from which average density and average compressibility are deduced from the bulk phase properties and from the volumetric liquid fraction  $\phi_l$ . The sound velocity predicted on the basis of these effective quantities, called Wood's velocity, is in good agreement with the experimental observations for bubble size below a frequency dependent critical value.<sup>9,10</sup> Above this bubble size, a resonant behaviour is observed: the energy absorption and the sound velocity reach maximal values.<sup>11,12</sup> In this regime, the liquid and gas phases, having very different inertia, do not follow the same trajectory and the simple continuum approximation made in Wood's model is not valid anymore. Finally in the large bubble size limit, most of the liquid phase stays at rest, as proposed by Kann's model,<sup>13</sup> and the velocity decreases toward its Kann's value, still larger than the Wood's prediction. These different models focus on the local deformations and motions induced by the pressure wave, but do not model the resulting energy dissipation. This dissipation is simply neglected in Wood's and Kann's models and taken into account by a single phenomenological internal time scale in the resonant model.<sup>12</sup>

Other studies focused in contrast on the fundamental origin of the energy dissipation. For a single bubble in an unbounded liquid, Prosperetti first modeled the high thermal dissipation induced by the large contact area between the gas phase, which temperature varies with the pressure, and the liquid phase, which remains at constant temperature.<sup>14,15</sup> This model has been used for foams in ref. 9 and 16, assuming a continuum deformation, as in Wood's regime. The thermal dissipation model predicts a maximum of dissipation for a given bubble size, as the resonant model. In this paper, we present results on the propagation of a short overpressure, characteristic of a blast wave, in a liquid foam. We measure the pulse velocity and the maximal pressure attenuation, as a function of the bubble size  $R$ , the liquid fraction  $\phi_l$ , the initial pressure amplitude  $P_1$  and the nature of the gas. This strongly broadens the parameter space already explored in our previous paper,<sup>16</sup> in which a single gas and a single liquid fraction had been used. It thus allows us to establish two important results: (i) the pressure attenuation depends on the nature of the gas, and that (ii) a maximum of attenuation is obtained for a critical bubble size, at a fixed liquid fraction. The first one is a very discriminant piece of information in order to build the right model of dissipation, whereas the second one may be useful to optimise the foam properties for practical use. Comparison with both resonant and thermal models allows us to conclude that the observed maximum of dissipation is due to the non monotonic variation of the thermal dissipation in the gas phase with the bubble size.

## 2 Experimental setup

In all experiments described in this paper, a foam is subject to a blast wave. In this section, we describe the foaming solution

*Institut de Physique de Rennes, UMR 6251 CNRS/Université de Rennes 1, Rennes, France. E-mail: isabelle.cantat@univ-rennes1.fr*

Table 1 Gas properties of  $N_2$  and  $C_2F_6$ <sup>17</sup>

Property	$N_2$	$C_2F_6$
Density $\rho_g$ ( $kg\ m^{-3}$ )	1.18	5.84
Thermal conductivity $\kappa$ ( $W\ m^{-1}\ K^{-1}$ )	0.024	0.0135
Specific heat $c_p$ ( $J\ kg^{-1}\ K^{-1}$ )	1040	760
Molar mass $M$ ( $g\ mol^{-1}$ )	28.0	138.0
Thermal diffusivity $D_T$ ( $10^{-5}\ m^2\ s^{-1}$ )	1.95	0.304

and gas (Section 2.1), the foam production and characterisation (Section 2.2), the blast wave generation and the pressure measurements (Section 2.3) and the measurement of the wave velocity (Section 2.4).

## 2.1 Foaming solution and gas

The foam is produced with a solution of sodium dodecyl sulfate (SDS) at a concentration of  $10\ g\ L^{-1}$ , larger than the critical micellar concentration (cmc) which equals  $2.8\ g\ L^{-1}$ . The gas is either nitrogen ( $N_2$ ) as in ref. 16, or hexafluoroethane ( $C_2F_6$ ). The thermal properties of these two gases are reported in Table 1.

## 2.2 Foam production and characterisation

The two experimental set-ups used in this paper are denoted by V and H (as vertical and horizontal).<sup>16</sup>

In set-up H, the foam is produced by a turbulent mixing method<sup>18</sup> and injected between two horizontal plexiglass plates separated by a distance  $h$ . The liquid fraction is controlled by the balance between the gas and solution flow rates and pressures and can be varied over the range  $\phi_1 \in [0.02-0.3]$ . For each experiment, it is measured by weighing a known volume of foam. The initial bubble radius is constant and close to  $R = 30\ \mu m$ .

The foam coarsening leads to the bubble size increase and this parameter is thus tuned by changing the waiting time between the foam production and the blast. The set-up allows to vary independently the control parameters  $R$  and  $\phi_1$  over a certain range, limited by several processes. The waiting time  $\tau_c$  required to double the bubble radius varies as  $R^2/(DHe)$ , with  $He$  the Henry coefficient, which measures the gas solubility, and  $D$  the gas diffusivity in the liquid phase. This characteristic time is of the order of a few seconds for  $R = 30\ \mu m$  and  $N_2$ , and is much larger for  $C_2F_6$ , which is 30 times less soluble than  $N_2$ .<sup>19,20</sup> Moreover,  $\tau_c$  increases with liquid fraction. Another ageing process is gravitational drainage. The liquid phase begins to leave the foam and to leak on the bottom plate after a time  $\tau_{dr}$  scaling as  $1/R^2$  and decreasing with liquid fraction. The cell is thus turned upside down during the coarsening process at a frequency larger than  $1/\tau_{dr}$  to maintain a homogeneous liquid fraction. Finally, this set-up can be used when the total coarsening time is smaller than 15 minutes and the draining time larger than 10 seconds. The resulting maximal bubble radius is typically  $300\ \mu m$  for  $\phi_1 = 5\%$  and  $N_2$  foams.

To extend the accessible range of parameters, the set-up V has been designed. In that case, the foam is produced by blowing gas in porous glass frits immersed in the foaming solution (see Fig. 1) and the bubble size is modified by changing the porosity of the frits. The foam then rises between two vertical plexiglass plates,

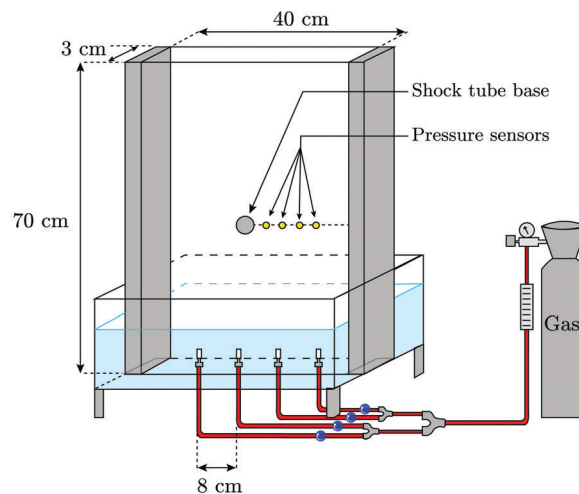


Fig. 1 Sketch of the vertical set-up. Pressure is monitored at the exit of the gas bottle and the flux in each frit is controlled by a valve (blue patches on the figure).

and overflows at the top of the cell. Once a steady state is reached, a sample of known volume of the foam is weighed to measure the liquid fraction as with H. The latter is governed by the upward foam velocity, and can be tuned by changing the inlet pressure, which controls the global flux in the frits. Additionally, the individual flux in each frit is controlled by a valve (see Fig. 1). Indeed, as the bubble size slightly depends on the flux through the frit, it is important to get the same flux in each frit. When the foam looks homogeneous, and while it is still flowing, it is subject to the blast wave.

We checked in ref. 16 for a given set of parameters that the pressure wave propagation is the same in set-up H and V. Results obtained with both set-ups can thus be directly compared.

For  $N_2$  foams, the bubble size distribution of each foam sample is measured by spreading a few hundred bubbles on top of a thin layer of the foaming solution. The bubbles form a monolayer of spherical bubbles and their radius distribution can be obtained by image processing.<sup>10</sup> The size of a bubble in the foam is thus measured by the radius  $R_s$  of the sphere of same volume.

For  $C_2F_6$  foams, the diffusion of the outside air into the bubbles is too fast to use this spreading method<sup>21</sup> and an *in situ* measurement must be performed. We record an image of the layer of bubbles touching the transparent plexiglass plate and the contact area between the bubbles and the wall is determined by image processing. A calibration has been done using both techniques with  $N_2$  foams to convert the contact area distribution into the  $R_s$  distribution. The average value  $R = \langle R_s \rangle_{\text{bubbles}}$  is the bubble radius used in the paper to characterise the bubble size in the foam. Each data point reported in this paper, at a target value of bubble radius, liquid fraction, blast strength, and gas, is the result of at least three independent experiments. All standard deviations and error bars come from the dispersion of the results of these individual experiments. The normalised standard deviation of the bubble distribution is close to 0.4 for all foams, which quantifies the foam polydispersity.

### 2.3 Blast wave generation and pressure measurements

A rigid PVC shock tube is connected at one end to the front plexiglass plate, in the middle of the plate (see Fig. 1). At the other end of the tube, a chamber is sealed by an aluminium foil, and connected to a gas bottle. To generate the pressure wave, we let the gas flow into this chamber; when the pressure in this chamber reaches a critical value, the foil breaks and a pressure wave propagates in the tube. A shock wave (*i.e.* a stiff pressure step followed by a finite interval of sustained high pressure) forms in the tube and evolves into a blast wave (*i.e.* a short overpressure followed by an underpressure) when exiting the tube. This blast wave then propagates in the foam. The pressure in the foam is recorded using four pressure sensors (PCB – piezotronics, model 113B28) installed at distances  $r_i = [3.1, 5.1, 7.2, 9.2]$  cm ( $i = 1$  to 4) from the symmetry axis of the experiment, corresponding to the center of the tube. They are connected to an oscilloscope (tektronics, model TDS 2004 B), which has a sampling time of 4  $\mu$ s. Fig. 2 shows typical signals at sensors 1 and 4. At sensor 1, a rapid pressure increase is followed by a slower pressure decrease and an underpressure, also called rarefaction wave. This kind of profile is known as a Friedlander profile.<sup>22,23</sup> The duration of the pressure increase is of the order of 0.1 ms, which is about 100 times larger than the nominal pressure sensor rise time. The duration of the overpressure is of the order of 2 ms. We observed that these two characteristic quantities do not depend on the foam, and that the shape of the pressure signals are quite reproducible (Fig. 2). Henceforth, for the sake of simplicity, we will thus consider that the pressure wave is entirely determined by its maximal value at sensor 1, denoted by  $P_1$  in the following. It is varied by changing the number of aluminium foils used to close the high pressure chamber. The maximal value recorded at sensor 4 is  $P_4$  and we define the pressure ratio as  $\alpha = P_4/P_1$ . The first reflection of the wave on the external boundary of the foam reaches the sensor 4 at  $t \approx 5$  ms, leading to a second overpressure. We only consider events occurring before this first reflection.

To test the influence of the cell geometry, we compared pressure signals obtained from pairs of sensors placed at the same distance from the center, respectively on the top and the bottom plates, with a 3 cm gap, in the H geometry. At the position

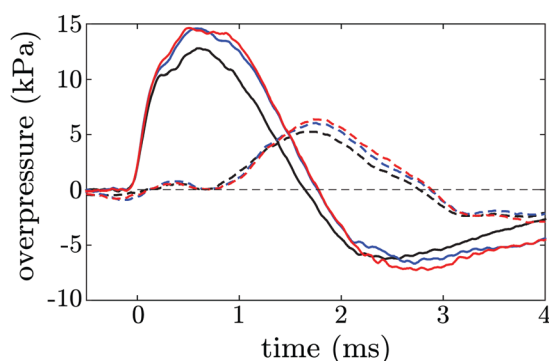


Fig. 2 Typical pressure signals in a  $C_2F_6$  foam measured at sensor 1 and sensor 4, for  $R = 422$   $\mu$ m and two aluminium foils. The time origin corresponds to the arrival of the blast wave on sensor 1.

of the first sensor ( $r \approx 3$  cm), the bottom signals amplitudes are always greater than the top ones by a factor in the range [1–1.5]. However both signals always superimpose at the position of sensor 4 ( $r \approx 9$  cm), with differences smaller than the experimental reproducibility. We also varied the H cell thickness from 1.7 cm to 8 cm. The pressure decrease from sensor 1 to sensor 4 (on the top plate) was not modified for gaps between 1.7 cm and 3 cm. For larger gaps, a faster decrease was observed, interpreted as a transition from a cylindrical (at small gap) to a spherical (at large gap) wave propagation. In Appendix A, we present comparisons between the pressure decreases obtained with the 3 cm and 8 cm gaps which confirm quantitatively this interpretation, thereby ensuring that geometrical effects have been correctly taken into account in the following data and interpretations.

In the following, we present experiments made in the cylindrical regime, with a 3 cm gap both in the H and V geometries.

### 2.4 Wave velocity measurements

The pressure wave deforms during its propagation, because of the non-linearities and of the viscous and dispersive nature of the medium (see Fig. 2). The wave velocity can thus be defined in different ways, leading to slightly different results. Experimentally, the maximal pressure  $P_i$  is well defined on the pressure signal  $i$ , but its arrival time is difficult to determine accurately, as it turned out that the signal is quite flat around the maximum. In contrast, the arrival time of the pressure  $P_i/2$ , denoted by  $t_{1/2,i}$  is a well defined quantity. We thus define the wave velocity as  $v = (r_4 - r_1)/(t_{1/2,4} - t_{1/2,1})$ .

In parallel to a velocity based on the pressure signals, optical measurements can also be performed. In that case, the foam sample is lit with an intense white light, used in transmission. The foam dynamics are recorded using a high-speed camera (Photron FastCam SA3), which is triggered by the same signal as the pressure sensors: both measurements are therefore synchronised. The dynamics remaining axisymmetric, we reduced the field of view to a narrow rectangle ( $640 \times 32$  pixel<sup>2</sup>), allowing to record images at 57 000 frames per second. A spatio-temporal diagram is obtained from the images, on which different gray levels are clearly visible, produced by the spatial fluctuations of the transmission coefficient of the foam (see Fig. 14 in Appendix B). Before the pressure wave arrives, these fluctuations are static and vertical lines are thus visible on the diagram. The sudden inflection of these lines at a position  $r$  and time  $t^{im}(r)$  is the signature of the pressure wave front reaching the position  $r$ . The wave velocity is deduced from the value  $t^{im}(r)$  as detailed in Appendix B.

Both definitions of the wave velocity, based on the pressure signals or on light transmission, are equivalent, as evidenced in Fig. 14, Appendix B.

With the optical measure, we get the front velocity at any position during the propagation. For  $r < r_1$  a high velocity transient is observed (see Fig. 14, Appendix B), but the velocity becomes independent on  $r$  for  $r > r_1$  in all our experiments. This steady velocity increases with  $P_1$ , as expected for a non-linear propagation.<sup>16</sup> However, for  $P_4 < 10$  kPa, the wave

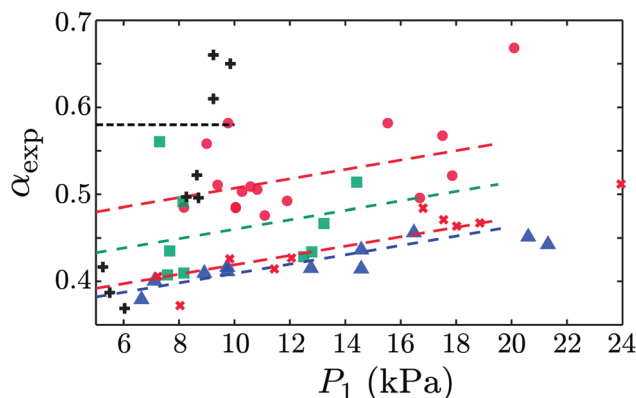


Fig. 3 Pressure attenuation as a function of the shock amplitude.  $\text{C}_2\text{F}_6$  foams:  $\bullet$   $R = (218 \pm 5) \mu\text{m}$ ,  $\phi_l = (5.6 \pm 0.5)\%$ ;  $\blacktriangle$   $R = (422 \pm 13) \mu\text{m}$ ,  $\phi_l = (4.4 \pm 0.4)\%$ ;  $\blacksquare$   $R = (794 \pm 28) \mu\text{m}$ ,  $\phi_l = (4.2 \pm 0.3)\%$ .  $\text{N}_2$  foams:  $\times$   $R = 210 \mu\text{m}$ ,  $\phi_l = (4.8 \pm 0.3)\%$  (already published in ref. 16, Fig. 3);  $+$   $R = 840 \mu\text{m}$ ,  $\phi_l = (4.9 \pm 0.2)\%$ . Black dashed line: geometrical attenuation corresponding to a cylindrical propagation. Coloured dashed lines: affine fits with the imposed slope  $k_0 = 5.4 \times 10^{-3} \text{ kPa}^{-1}$ .

velocity variation due to the pressure is smaller than the experimental dispersion. Therefore, the velocities discussed in the following are the average over all the experiments we performed which verifies  $P_4 < 10 \text{ kPa}$ .

## 3 Results

### 3.1 Influence of the gas and of the bubble radius

The set-up V was used with glass frits of three different calibrated porosities 2, 1 and 0 to produce a  $\text{C}_2\text{F}_6$  foam with bubble radii in the range 200 to 800  $\mu\text{m}$ . The pressure attenuation and the wave velocity are measured as a function of the bubble radius and of the pressure amplitude. To allow comparison with the previous study on  $\text{N}_2$  foams,<sup>16</sup> the liquid fraction  $\phi_l$  was adjusted as close as possible to 4.8% by tuning the gas flux through each frit. The bubble radius range of the previous study was also enlarged by adding a point at  $R = 840 \mu\text{m}$  for a  $\text{N}_2$  foam.

**3.1.1 Wave attenuation.** We report in Fig. 3 the pressure ratio  $\alpha_{\text{exp}} = P_4/P_1$  as a function of  $P_1$  obtained for these experiments, and one data series from Fig. 3 in ref. 16, for sake of comparison. The pressure ratio increases with the pressure intensity. This behavior has been reproduced numerically by a slightly nonlinear numerical model in ref. 16. These simulations show an almost affine behavior, with a slope independent on the material attenuation. The extrapolation at  $P_1 = 0$  is in contrast a signature of the attenuation properties, and the remaining part of the paper will thus focus on this extrapolated value. The affine fits at constant slope are indeed in good agreement with the data, even if a quantitative comparison is made difficult by the large experimental noise observed with some series. Only the  $\text{N}_2$  foam with the largest bubble radius ( $R = 840 \mu\text{m}$ ) is not compatible with such a fit as it exhibits a much faster increase of  $\alpha_{\text{exp}}$  with  $P_1$ . This last data series corresponds to a different regime, as discussed in Section 4 and is first discarded in the following discussion.

An important result of this paper is that the pressure ratio  $\alpha$  depends on the nature of the gas. A direct comparison can be made in Fig. 3 for  $R \simeq 210 \mu\text{m}$ : the pressure ratio is significantly larger with  $\text{C}_2\text{F}_6$  than with  $\text{N}_2$  over the whole pressure range, which is the proof of a smaller attenuation with  $\text{C}_2\text{F}_6$ . This is a crucial hint to determine the fundamental nature of the dissipation processes leading to the wave attenuation. Indeed, as the bubble radius, the liquid fraction and the surfactants are the same for both series, the dissipation in the liquid phase and at the interfaces is not modified and thus cannot explain the attenuation variation between both series. This evidences that the dissipation in the gas itself contributes significantly to the total dissipation.

Moreover, for all  $P_1$  values, the pressure ratio for  $\text{C}_2\text{F}_6$  foams first decreases with the bubble radius and then increases at larger bubble radius. This surprising non-monotonous behaviour is discussed in the next paragraph.

**3.1.2 Attenuation length.** In the small amplitude regime, and in a non-dissipative, non-dispersive medium, the pressure attenuation only depends on the space dimension. A propagation with a cylindrical symmetry induces a pressure ratio  $\alpha_{2D}^{\text{ref}}(r) = \sqrt{r_1/r}$  between two points at the distance  $r$  and  $r_1$  of the symmetry axis. Dissipation in the medium will induce an additional pressure decrease which can be characterised in the linear regime by an attenuation length  $\ell_a$ . The pressure ratio is in this case  $\alpha(r) = \alpha^{\text{ref}} e^{-(r-r_1)/\ell_a}$ . The attenuation length is the intrinsic property of the material, which must be measured to quantify attenuation.

To measure  $\ell_a$ , we extrapolated at  $P_1 = 0$  the affine fits made in Fig. 3 to obtain the experimental value of  $\alpha$  (for  $r = r_4$ ) in the low pressure limit, *i.e.* in the linear regime. The low pressure data of each series ( $P_1 < 20 \text{ kPa}$ ), including those of Fig. 3 in ref. 16, were first fitted by the law  $\alpha = k_1 P_1 + k_2$ , with  $k_1$  and  $k_2$  fitting parameters which depends on the bubble size  $R$  and on the nature of the gas  $g$ . The obtained slopes  $k_1$  were then averaged over all the series (excepted the  $\text{N}_2$  series at  $R = 840 \mu\text{m}$ ), leading to  $k_0 = \langle k_1 \rangle_{R,g} = 5.4 \times 10^{-3} \text{ kPa}^{-1}$ . The different series were finally fitted by the one-parameter law  $\alpha_{\text{exp}} = k_0 P_1 + \alpha_0(R,g)$ , as shown in Fig. 3. The experimental attenuation length is finally given, for each bubble radius and each gas, by

$$\frac{1}{\ell_a^{\text{exp}}} = \frac{1}{r_4 - r_1} \ln \frac{\sqrt{r_1/r_4}}{\alpha_0(R,g)}. \quad (1)$$

As discussed in Appendix A, more data points have been obtained in spherical propagation geometry, and they were found to be consistent with the data obtained with a cylindrical propagation.

Fig. 4 shows  $1/\ell_a$  as a function of the bubble radius, for the two gases. As discussed in the previous section, the attenuation is larger in  $\text{N}_2$  foams than in  $\text{C}_2\text{F}_6$  foams in the investigated bubble radius range. The non-monotonous behaviour of the  $\text{C}_2\text{F}_6$  foams appears more clearly in this representation: the attenuation in  $\text{C}_2\text{F}_6$  foams exhibits a maximum for a bubble radius around 500  $\mu\text{m}$ , as was conjectured in ref. 16 for  $\text{N}_2$  foams. This result is important for practical reasons, as the optimal



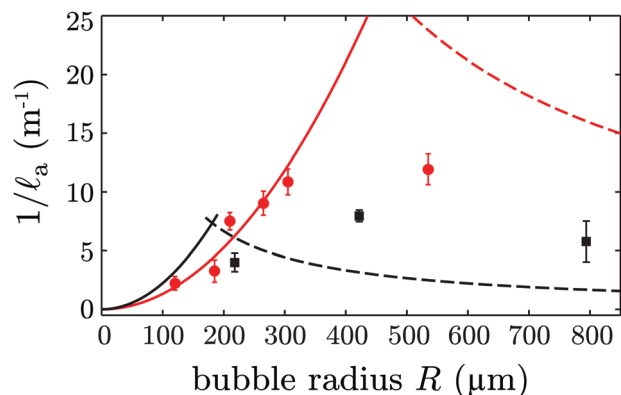


Fig. 4 Attenuation length for  $\text{C}_2\text{F}_6$  foams (■) and for  $\text{N}_2$  foams (●), as a function of the bubble size, for a liquid fraction  $\phi_l = 4.8\%$ . Solid lines: prediction of eqn (3) (isothermal regime), with the prefactor  $\lambda_T = 0.4$  for both gases (red:  $\text{N}_2$ , black:  $\text{C}_2\text{F}_6$ ). Dashed lines: predictions of eqn (4) (adiabatic regime) with  $\lambda_a = 12$ , for both gases.

pressure attenuation is sought in many applications. It is also a very discriminant experimental information to test different theoretical models of dissipation, as discussed in Section 4.

**3.1.3 Wave velocity.** The velocity  $v$  of the pressure wave front is plotted in Fig. 5 as a function of the bubble radius. The velocity in the  $\text{C}_2\text{F}_6$  foams (same experiments as in Fig. 4) is shown in the top graph and was measured from the pressure signal. One additional point at  $R = 45 \mu\text{m}$  has been obtained in cell H at large gap (spherical propagation). As the wave velocity is independent on the geometry, this data point can be compared to the other ones. The velocities for the  $\text{N}_2$  foams have

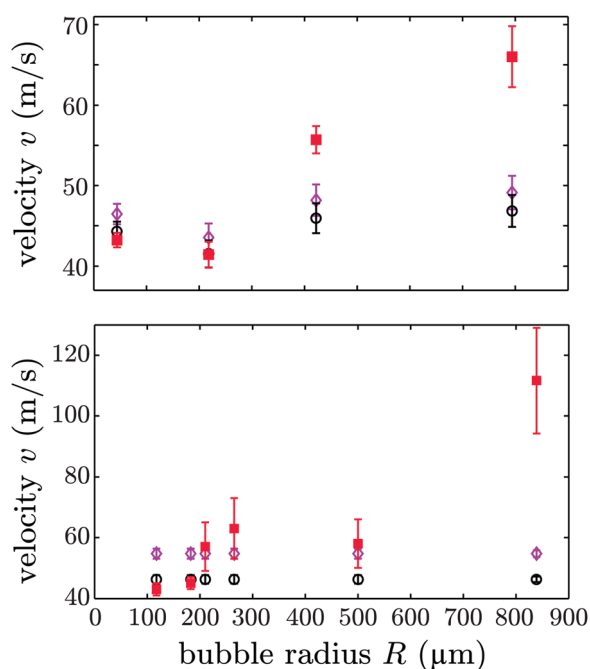


Fig. 5 (Top) Wave front velocity for  $\text{C}_2\text{F}_6$  foams as a function of the bubble radius for  $\phi_l = 4.8\%$  (■). Theoretical Wood's velocity given by eqn (2) for isothermal (○) and adiabatic (◇) regimes. (Bottom) Wave front velocity for  $\text{N}_2$  foams and Wood's predictions, same symbols.

been measured on the images (same experiments as in ref. 16), close to sensor 4. The point at  $R = 840 \mu\text{m}$  is a new experiment, with a velocity measured with the pressure signal.

A classical prediction for the wave velocity in the linear regime is Wood's velocity.<sup>8</sup> This model assumes that the foam behaves as an effective medium of compressibility  $\chi_0$  and density  $\rho_0$ , averaged over the volume fractions of the liquid and the gas phases. As the liquid phase is almost incompressible,  $\chi_0$  is based on the gas compressibility:  $\chi_g = 1/(\bar{\kappa}p_0)$ , leading to  $\chi_0 = (1 - \phi_l)/(\bar{\kappa}p_0)$ , with  $\phi_l$  the liquid fraction measured at the atmospheric pressure  $p_0$ , and  $\bar{\kappa}$  the polytropic exponent.<sup>14</sup> The gas is modeled as an ideal gas with  $\bar{\kappa} = \gamma$  or  $\bar{\kappa} = 1$  for an adiabatic or isothermal compression, respectively. Here,  $\gamma$  is the ratio of specific heats; it equals 1.4 for  $\text{N}_2$ , and 1.085 for  $\text{C}_2\text{F}_6$ .<sup>24</sup> The foam density is given by  $\rho_0 = \phi_l\rho_s + (1 - \phi_l)\rho_g$  where  $\rho_s$  and  $\rho_g$  are respectively the solution and gas densities.<sup>8,25</sup> Wood's velocity is thus:

$$c_w^2 = \frac{1}{\chi_0\rho_0} = \frac{\bar{\kappa}p_0}{1 - \phi_l} \frac{1}{\phi_l\rho_s + (1 - \phi_l)\rho_g}. \quad (2)$$

The adiabatic and isothermal Wood's velocities  $c_{w,a}$  and  $c_{w,T}$  have been computed for each experiment, on the basis of the measured liquid fraction  $\phi_l$ . The obtained values are reported in Fig. 5. The experimental wave velocities remain close to Wood's velocities for small bubbles, and become larger than this prediction for bigger bubbles. The velocity is indeed 2.5 times larger than Wood's prediction for the largest bubble radius and the  $\text{C}_2\text{F}_6$  foam, and it reaches twice the predicted value for the  $\text{N}_2$  foam with the largest bubble radius. This last sample is the one which also shows a specific behaviour in Fig. 3. A departure from Wood's velocity is a strong indication that a gas bubble and its contiguous liquid environment do not move with the same amplitude when the pressure wave arrives. The menisci, *i.e.* the liquid channels at the intersection of three films, having a much larger inertia than the thin films, have a different dynamics than the gas and the films. This effect is at the basis of the resonance observations and models established in ref. 11 and 12 and becomes important above a critical bubble radius.

Fig. 5 shows that for the bubble radius corresponding to the maximum of dissipation, *i.e.*  $R \approx 450 \mu\text{m}$ , the wave velocity is still close to the Wood's velocity. This is a first indication that the maximum cannot be explained by the resonance.

### 3.2 Influence of the liquid fraction

The influence of the liquid fraction has been investigated for  $\text{N}_2$  foams in the large bubble limit ( $R$  close to  $900 \mu\text{m}$ ) using the setup V and in the small bubble limit ( $R$  close to  $95 \mu\text{m}$ ) using the setup H. The shock was always produced with a single aluminum foil (low pressure range). For both series, the velocity is measured from the pressure signals.

**3.2.1 Wave attenuation.** The pressure ratio for large bubbles is plotted in Fig. 6 and shows a decrease of  $\alpha$  with the liquid fraction, *i.e.* an increase of attenuation. For a given frit porosity, the bubble radius fluctuates over a certain range and we kept only the experiments with bubble radius in the range  $800$  to  $950 \mu\text{m}$ . The bubble radius is indicated for each data point by a

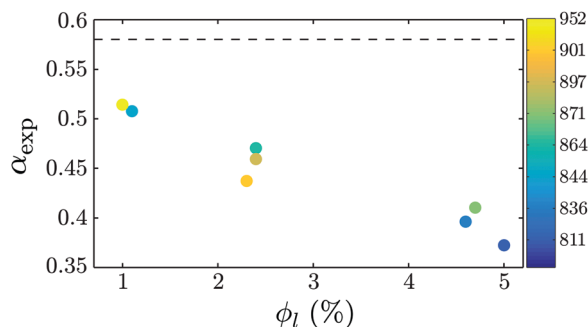


Fig. 6 Pressure ratio  $\alpha_{\text{exp}} = P_4/P_1$  as a function of the liquid fraction  $\phi_l$  for a  $\text{N}_2$  foam in the V cell. Colours indicate the bubble radius in micrometer for each experiment. The average radius is  $R = 870 \mu\text{m}$ . The dashed line represents the pressure ratio  $\alpha^{\text{ref}}$  associated to the geometrical attenuation.

colour code in Fig. 6. For the different liquid fractions, the largest value of  $\alpha$  is obtained either for the smallest or for the largest bubble sizes. For bubbles larger than  $900 \mu\text{m}$ , we expect that  $\alpha$  increases with the bubble size (see Fig. 3), but the bubble size scatter in this figure is small enough for this dependency to be unobservable. The variation of  $\alpha$  is thus solely due to the liquid fraction variation. Similarly, we only kept  $P_1$  values in the range 4.8 to 6 kPa. From the value of  $\alpha$ , we deduce the attenuation length of the foam using eqn (1), shown in Fig. 9. As the pressure intensity has not been varied, the pressure ratio cannot be extrapolated to  $P_1 = 0$ , and the parameter  $\alpha_0$  in eqn (1) is identified with the raw data  $\alpha^{\text{exp}}$ .

The same study was performed for small bubble radius, as shown in Fig. 7. In that case, the pressure attenuation is equal to the geometric attenuation, within the experimental error bars. This means that the attenuation due to the medium itself is not detected. We can therefore not conclude about a potential dependency with the liquid fraction in this small bubble regime. This result also confirms that foams with small bubbles do not attenuate much sound waves, in agreement with Fig. 4 and 13.

**3.2.2 Wave velocity.** The wave velocity measured from the pressure signals is reported in Fig. 8 as a function of the liquid fraction for small bubble radii ( $R = 95 \mu\text{m}$ , same experiments as in Fig. 7) and for large bubble radii ( $R = 870 \mu\text{m}$ , same experiments

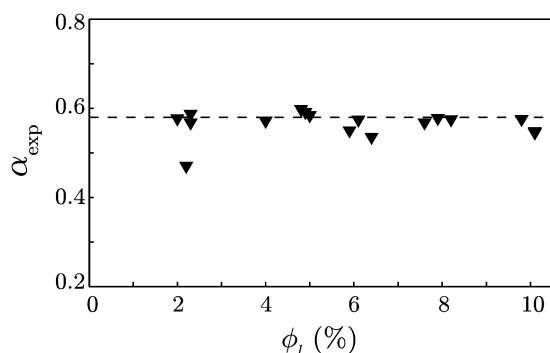


Fig. 7 Attenuation  $\alpha = P_4/P_1$  for a bubble radius  $R = (95 \pm 13) \mu\text{m}$ , obtained for a  $\text{N}_2$  foam in the H cell. The dashed line is the geometrical attenuation.

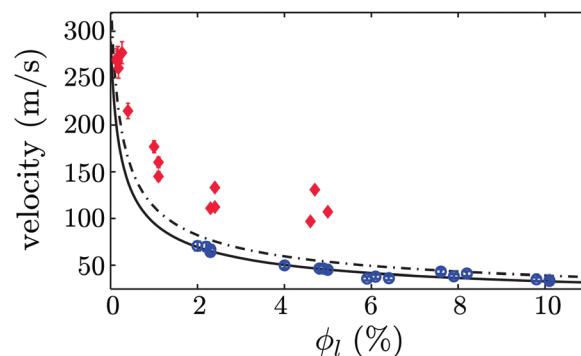


Fig. 8 Wave front velocity for  $\text{N}_2$  foams as a function of the liquid fraction, deduced from the pressure signals. (●) Small bubble radius:  $R = 95 \mu\text{m}$  (same experiments as in Fig. 7); (◆) large bubble radius:  $R = (870 \pm 44) \mu\text{m}$  for  $\phi_l > 1\%$  (same experiments as in Fig. 6) and  $R$  in  $[900-1100] \mu\text{m}$  for  $\phi_l < 1\%$ . Wood's prediction is represented with a full line for the isothermal regime, and dashed line for adiabatic regime. The data at  $\phi_l = 4.8\%$  have already been shown in Fig. 5.

as in Fig. 6, and additional points at  $\phi_l < 1$  with  $R$  in the range 900 to  $1100 \mu\text{m}$ ). Wood's velocities for an adiabatic and an isothermal propagation (eqn (2)) are plotted on the same graph, without fitting parameter. A very good agreement is obtained between the small bubble series and the isothermal Wood's velocity, whereas for the large bubble the experimental velocities are larger than Wood's velocity by a factor which reaches 2.5 for  $\phi_l$  close to 5%. This confirms that the wave propagation is in the Wood regime at small bubble size, and departs from it at larger bubble size. The transition is difficult to quantify, but Fig. 5 indicates that it is around  $R = 800 \mu\text{m}$ .

## 4 Models

### 4.1 Thermal dissipation model

The thermal model developed in ref. 9, 14 and 15 and already used in ref. 16 assumes that the energy dissipation is mainly of thermal origin. The gas in the bubbles is compressed by the pressure wave, its temperature thus increases and dissipative heat transfers occur between the gas phase and the liquid phase, the latter acting as a thermostat. Such dissipation is strongly enhanced in foams because of the large contact area between the liquid phase and the gas phase, which temperatures differ strongly after the sharp pressure increase. At the end of the overpressure, the gas is thermalised by the liquid on a shell of thickness  $\ell_T = \sqrt{D_T \tau}$  around each gas bubble, with  $D_T$  the heat diffusivity given in Table 1 and  $\tau$  the overpressure duration. For  $\tau = 2 \text{ ms}$  (Fig. 2), we thus compute  $\ell_T = 200 \mu\text{m}$  for  $\text{N}_2$  and  $80 \mu\text{m}$  for  $\text{C}_2\text{F}_6$ . A priori, if the bubble radius  $R$  is much smaller than  $\ell_T$ , the propagation is almost isothermal, and in the other limit, the process is almost adiabatic. The attenuation lengths in these two regimes are respectively:<sup>16</sup>

$$\frac{1}{\ell_a^T} = \lambda_T \frac{R^2 c_{w,T} \rho_0}{\kappa T \tau^2}, \quad (3)$$

$$\frac{1}{\ell_a^A} = \lambda_A \frac{c_{w,A} \rho_0}{\rho_g c_p T R \sqrt{\frac{\kappa}{\rho_g c_p \tau}}}, \quad (4)$$

with  $T$  the temperature,  $c_{w,A}$  and  $c_{w,T}$  the wave velocities for adiabatic and isothermal propagations given by eqn (2),  $\rho_0$  the foam density and  $\kappa$ ,  $c_p$  and  $\rho_g$  the gas properties given in Table 1. The parameters  $\lambda_A$  and  $\lambda_T$  are dimensionless fitting parameters, and all the other quantities are known for the two gases. A direct comparison with our experimental data can thus be made, to identify the origin of the observed dependencies with the liquid fraction, the bubble radius and the nature of the gas.

The model predicts an attenuation  $1/\ell_a$  which increases with the liquid fraction  $\phi_l$ , both in the small and large bubble radius limits. Indeed, even if this model considers only a dissipation in the gas phase,  $1/\ell_a$  depends on the liquid fraction through Wood's velocity, scaling as  $\phi_l^{-1/2}$ , and through the foam density scaling as  $\phi_l$ . The attenuation lengths deduced from the pressure ratios shown in Fig. 6 ( $N_2$  foam) are plotted in Fig. 9. As the bubble radius for these data is  $R = 870 \mu\text{m}$ , which is in the large bubble regime, they are compared with the prediction in the adiabatic regime. Fig. 9 shows a good agreement between the experimental data and the prediction of eqn (4) for a prefactor  $\lambda_A = 5$ . This value is close to the value  $\lambda_A = 7$  used in ref. 16 to reproduce the experimental data obtained with  $N_2$  foams.

The dependency of  $1/\ell_a$  with the bubble radius predicted by the model is more complex. It predicts an increase of the attenuation as  $R^2$  for small bubbles (eqn (3)), followed by a decrease as  $1/R$  for large bubbles (eqn (4)). We show in ref. 16 that the attenuation in  $N_2$  foams is well fitted by this model for the couple of parameters ( $\lambda_T = 0.4$ ;  $\lambda_A = 7$ ). The prefactor  $\lambda_A = 7$  is too small to reproduce the data at large bubbles of Fig. 4, obtained with  $C_2F_6$ , that would be best fitted with  $\lambda_A$  close to 35. The prediction of the model using the couple of parameters ( $\lambda_T = 0.4$ ;  $\lambda_A = 12$ ), chosen as a best compromise between the two gases, is shown in Fig. 4 together with the experimental data.

All important qualitative features are reproduced by this thermal model, despite the lack of quantitative agreement: a maximum of attenuation is observed for a bubble radius close to the thermal length; the attenuation is smaller for  $C_2F_6$  foams than for  $N_2$  foams in the investigated parameter range; the order of magnitude of the predicted attenuation is in the right range; the attenuation increases with the liquid fraction at large bubble radius.

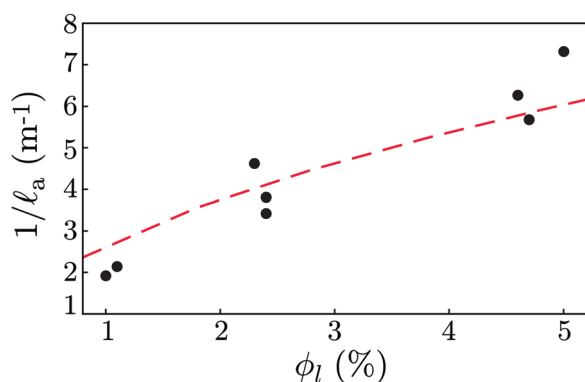


Fig. 9 Attenuation length as a function of the liquid fraction (same data as in Fig. 6). The red dashed line is the prediction of the thermal model in the adiabatic regime (eqn (4)) with a prefactor  $\lambda_A = 5$ .

This allows to conclude that the thermal dissipation is non-negligible in the investigated parameter range, and that it is probably at the origin of the observed maximum of attenuation. The discrepancy between the model and the experiment may be explained by the fact that other dissipative and dispersive processes also contribute to the global pressure attenuation, with different scaling laws. For instance, viscous effects within the liquid phase, which are ubiquitous in foam rheology,<sup>26</sup> are also expected to play a role. The thermal model itself could be refined: in particular, the liquid films are so thin that the assumption that they act as thermostats is questionable, especially at large bubble size.

Furthermore, the thermal model implicitly assumes the validity of Wood's prediction. The velocity increase at large bubble radius is thus not predicted in this model, and is potentially related to the proximity of the resonant behaviour evidenced in ref. 11 and 12, as discussed in the next section.

## 4.2 Resonant film-meniscus model

Wood's model is based on the assumption that the foam behaves as a continuum and that, locally, the gas, the liquid in the films and the liquid in the menisci move at the same velocity  $\vec{v}(\vec{r}, t)$ , which varies at the scale of the acoustic wavelength. However, at very large frequencies, the menisci do not move any more, and only the thin films, with a much smaller inertia, are displaced by the pressure wave.<sup>13</sup> Pierre *et al.* recently gave an extensive description, both theoretical and experimental, of the transition from one regime to another, at a critical frequency (for a given bubble radius)<sup>12</sup> or at a critical bubble radius (for a given frequency).<sup>27</sup> This transition coincides with a maximum of dissipation and occurs for parameter values (bubble radius, time scale...) close to our experimental parameter range. More precisely, Fig. 3 in ref. 12 shows that Wood's regime breaks down for a frequency  $f$  such that  $f(R/R_0)^{1.5} = 10^5$  Hz, with  $R_0 = 40 \mu\text{m}$ . Since the overpressure duration is in the ms range, it corresponds to typical frequencies in the kHz range. With  $f = 1$  kHz, we thus obtain that Wood's regime breaks down at  $R = 0.9$  mm, in agreement with our data on velocity (Fig. 5). It may thus *a priori* explain the maximum of dissipation which we observe, and is an alternative to the thermal model that must be carefully analysed. In contrast with the previous approach, this maximum of dissipation is not related to an especially efficient dissipative process at the bubble scale, but to an enhanced deformation of the film/meniscus structure. In this case, the dissipation is assumed to occur mainly in the connection between films and menisci and is simply modelled by a phenomenological time scale  $\tau_d$ , that does not depend on the bubble radius, nor on the frequency. The model developed in ref. 12 predicts a specific dispersion relation for the plane wave propagation, in the linear regime. In order to compare our observations with the predictions of this model, we computed the propagation of a pressure pulse using this dispersion relation. The incoming signal, at the position  $z = 0$ , is assumed to be  $p_1 = \sin(\pi t/\tau)$  for  $t \in [0, \tau]$  and 0 elsewhere, with  $\tau = 1$  ms the duration of the overpressure. This ansatz mimics well the shape of the overpressure signal at sensor 1 (Fig. 2), apart from its slight asymmetry, and neglects

the rarefaction wave. With this simplified form, the Fourier transform of the signal has an analytical expression, namely

$$\hat{p}(\omega) = \int_0^\tau e^{i\omega t} \sin\left(\frac{\pi t}{\tau}\right) dt \quad (5)$$

$$= \frac{2\pi\tau}{\pi^2 - \omega^2\tau^2} e^{i\omega\tau/2} \cos\left(\frac{\omega\tau}{2}\right). \quad (6)$$

The main Fourier components are in the range  $[0, 3\pi/\tau]$ , i.e. for  $\omega$  smaller than  $10^4 \text{ s}^{-1}$ . The pressure at distance  $z$  can then be determined by the relation

$$p(t, z) = \frac{1}{\pi} \text{Re} \left\{ \int_0^\infty \hat{p}(\omega) e^{-i[\omega t - k(\omega)z]} d\omega \right\}. \quad (7)$$

The dispersion relation which we used is based on eqn (2) in ref. 12:

$$k(\omega)^2 = \frac{\omega^2 \rho_{\text{eff}}}{p_0}, \quad (8)$$

with  $\rho_{\text{eff}} = (1 - \phi_l)\rho_g + \phi'_l \rho_s$  the foam effective density, built on the complex number  $\phi'_l$ , playing the role of an effective liquid fraction. It equals the actual liquid fraction at low frequency and Wood's velocity is recovered in this limit. In the high frequency limit, the liquid phase contained in the menisci does not move any more, and  $\phi'_l$  is the volumetric fraction of the thin films. This is the Kann regime.<sup>13</sup> In the intermediate regime, a resonant behaviour is observed, with a maximal modulus of  $\phi'_l$ . The full expression for  $\phi'_l$  is:<sup>12</sup>

$$\phi'_l = \frac{\phi_l}{1 + x^2 \frac{\phi_l}{\phi_f} [1 - \mathcal{H}(qa)] - i\omega\tau_d x \mathcal{H}(qa)}, \quad (9)$$

with  $q = \omega\sqrt{\rho_s e/(2\sigma)}$ ,  $e \sim 100 \text{ nm}$  the thin film thickness,  $\sigma = 36 \text{ mN m}^{-1}$  the surface tension,  $\tau_d = 10^{-5} \text{ s}$ ,  $x$  the fraction of the bubble area covered by the thin films, which equals 0.38 for  $\phi_l = 4.8\%$ ,<sup>28</sup> and  $a = \sqrt{x}R$  the radius of the thin film. The function  $\mathcal{H}(u) = 2J_1(u)/[uJ_0(u)]$  is built from the Bessel functions of order 0 and 1 and  $\phi_f = 3(1 - \phi_l)x^2e/(4R)$  is the volume of liquid contained in the thin films per unit foam volume. Using the approximate value for  $\mathcal{H}(u)$  for  $u \ll 1$ , a simple expression is obtained for the resonant frequency:  $\omega_r = \sqrt{12\sigma/(x^2\rho_s\phi_l R^3)}$ . For  $R = 500 \text{ }\mu\text{m}$ , this yields  $\omega_r = 2 \times 10^4 \text{ s}^{-1}$ , which is thus just above the highest frequencies of the incoming signal.

Fig. 10 shows the pressure signal at sensor 4 obtained with eqn (7) for bubble radius in the range 200 to 1100  $\mu\text{m}$ , for  $\text{N}_2$ . The signal is deformed due to the viscous and dispersive properties of the medium, but a well defined overpressure is still observable. The maximal pressure decreases with the bubble radius, as well as the slope of the initial pressure increase. However, the velocity deduced from  $t_{1/2}$  is almost independent of the bubble radius and remains close to Wood's velocity.

The attenuation length is obtained from the  $P_4/P_1$  ratio, using the relation  $\ell_a = (r_4 - r_1)/\ln(P_4/P_1)$ , because the simulated propagation is unidirectional, so there is no geometric attenuation. The experimental data of Fig. 3 are compared with the numerical attenuation length in Fig. 11, for three values of the

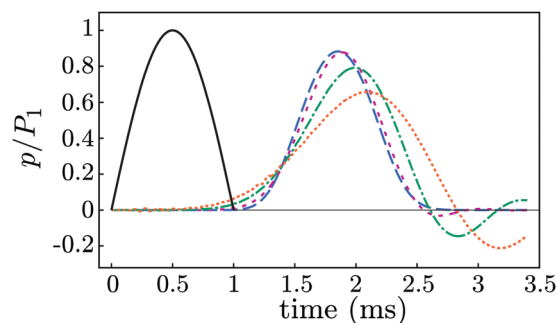


Fig. 10 Imposed pressure signal at the position  $z = 0$  as a function of time (black line) and pressure signal at the position  $z = 6 \text{ cm}$  determined numerically from eqn (7)–(9), for  $\text{N}_2$  and for the bubble radius  $R = (200, 500, 800, 1100) \text{ }\mu\text{m}$  (the attenuation increases with the bubble radius).

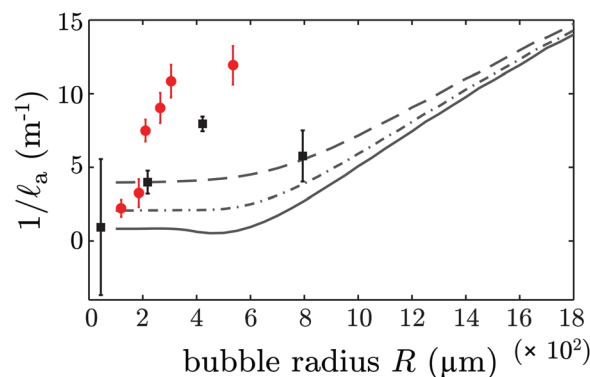


Fig. 11 Experimental attenuation length of Fig. 4 compared with the attenuation length obtained numerically for  $\text{N}_2$  and  $\tau_d = 2 \times 10^{-5} \text{ s}$  (solid line),  $5 \times 10^{-5} \text{ s}$  (dotted-dashed line) and  $10^{-4} \text{ s}$  (dashed line).

fitting parameter  $\tau_d$ , in the range  $[2-10] \times 10^{-5} \text{ s}$ . The results obtained numerically for  $\text{C}_2\text{F}_6$  are almost identical, as the density does not play a important role in the attenuation. As already visible in Fig. 10, the attenuation increases with the bubble radius. However it is impossible to explain the maximum of attenuation observed at  $R = 500 \text{ }\mu\text{m}$  with the resonant model. We checked that until at least  $R = 3 \text{ mm}$  (last computed value) the attenuation  $1/\ell_a$  keeps increasing with  $R$ . This strongly reinforces our conclusion that the thermal dissipation in the gas is at the origin of the observed maximum.

The resonant model nevertheless predicts the right order of magnitude of the attenuation length for bubble around  $800 \text{ }\mu\text{m}$ , and a transition from a thermal origin of the dissipation toward an origin based on the resonance model is possible. However, the wave velocity deduced from the numerical simulation varies by only 2% on the bubble radius range 200 to  $1100 \text{ }\mu\text{m}$ , so the fast velocity observed for  $\text{N}_2$  foams at  $R = 800 \text{ }\mu\text{m}$  remains unexplained.

Finally, we made the same comparison with the experimental data of Fig. 6, with a bubble radius  $R = 870 \text{ }\mu\text{m}$ . In that case, with a value of the adjustable dissipative time  $\tau_d \sim 5 \times 10^{-5}$  (to be compared with  $\tau_d = 10^{-5}$  obtained for another foam in ref. 12), the agreement with the prediction of the model is fair (see Fig. 12). As the thermal and resonant models both predict the increase of  $1/\ell_a$  with  $\phi_l$ , these data does not bring additional



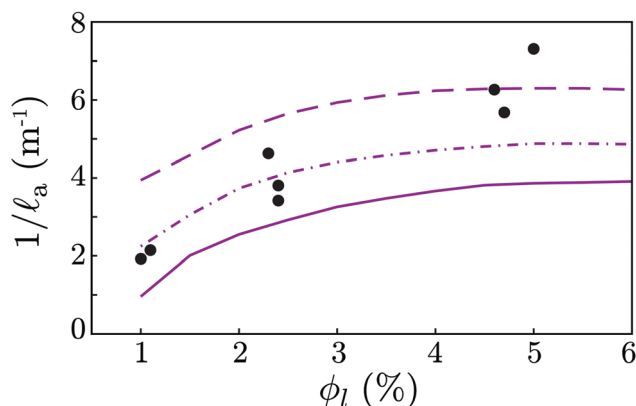


Fig. 12 Experimental data of Fig. 6 compared with the attenuation length obtained numerically for  $\tau_d = 2 \times 10^{-5}$  s (solid line),  $5 \times 10^{-5}$  s (dotted-dashed line) and  $10^{-4}$  s (dashed line).

information to discriminate between both models. However, the thermal model shown in Fig. 6 allows for a slightly better fit of the data.

## 5 Conclusions

In this paper, we have reported an extensive study of blast wave propagation and attenuation in liquid foams, mostly in the weak wave regime, where comparison with linear acoustics remains relevant. Thanks to our careful control of the foam production and parameters, we were able to study independently the influence of bubble size, liquid fraction, and gas. We showed for the first time that attenuation reaches a maximum for a certain bubble size, and depends on the gas. We also showed that attenuation increases at increasing liquid fraction.

These measurements of attenuation were compared to a model accounting for thermal dissipation in the gas phase in contact with the liquid interfaces. It reproduces all the aforementioned qualitative experimental features, although it does not yield a quantitative agreement with the data. The propagation velocity of the blast wave agrees with Wood's velocity at small bubble size, but becomes larger for bubble sizes above 0.5 to 0.8 mm. This is in qualitative agreement with a resonance model recently proposed.<sup>12</sup> We also showed that such a model could not explain the attenuation maximum.

These unprecedented results pave the way toward a more rational optimisation of shock and blast wave mitigation by liquid foams. It also opens several perspectives. First, we did not model the nonlinear regime, nor the dependence of attenuation on the blast wave amplitude. Second, and related to the first point, the possible destruction of part of the foam by a strong enough blast, and its influence on propagation and attenuation of the blast wave, remains to be addressed. We obtained some recent data along this direction, which will be presented in a subsequent study. We thus hope that the current study is a first but crucial bridge between the most recent developments of linear acoustics of liquid foams and the regime of strong shocks and blasts.

## Appendix A

In order to test our assumption of a cylindrical propagation in the 3 cm gap cell, we performed additional experiments in the H cell with a larger gap  $h = 8$  cm, with  $\phi_l = 4.8\%$  and  $R$  in the range 50 to 300  $\mu\text{m}$ . With this larger gap, it is clearly visible on the pressure signals that the maximal overpressure reaches sensor 4 before the first reflection on the bottom plate reaches the top plate. The signal measured by the sensor placed on the top plate is thus the same as a signal propagating in a half 3D space. As the foam was observed to slip at the top plate, we consider that the propagation is the same as in a full 3D space, and the reference attenuation  $\alpha_{3D}^{\text{ref}}(r) = r_1/r$  can be used. For this test, we have not systematically varied the overpressure. We assumed that the attenuation is of the form, at sensor  $i$ :

$$\alpha(r_i) = \frac{r_1}{r_i} \left( e^{-(r_i - r_1)/\ell_a} + K^{\text{sph}} P_1 \right) = \alpha_0(r_i) + k(r_i) P_1. \quad (10)$$

This involves an attenuation length  $\ell_a$ , which is the intrinsic material property we want to determine, the geometrical attenuation  $r_1/r_i$  which corresponds to a linear propagation in a spherical geometry, and the non-linear correction  $K^{\text{sph}} P_1$ . The slope  $K^{\text{sph}}$  is assumed to be independent of the bubble radius and of the nature of the gas, as in the cylindrical geometry (see Section 3.1.1). Its value  $K^{\text{sph}} = 7 \times 10^{-3} \text{ kPa}^{-1}$  has been determined from a single data set obtained at different pressure values with  $\text{C}_2\text{F}_6$ ,  $R = 45 \mu\text{m}$ , and  $r_i = r_3$ . This value is then used to compute the value of  $\alpha_0$  for all data obtained in the spherical geometry. The deduced attenuation lengths  $\ell_a$ , averaged over several data points for each bubble radius, is plotted in Fig. 13. The values are compatible with the ones obtained for the same gas  $\text{N}_2$  and same liquid fraction  $\phi = 4.8\%$  in the cylindrical geometry, thus confirming that the propagation between the two plates has a cylindrical symmetry, and that  $\ell_a$  does not depend on the cell geometry.

## Appendix B

A spatio-temporal diagram of the foam is shown in Fig. 14 (top). The gray level fluctuations produce vertical lines when the foam is at rest, and oblique curves when it moves. The transition between

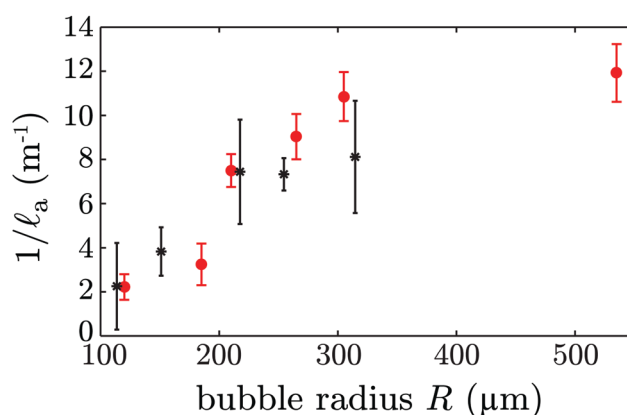


Fig. 13 Attenuation length as a function of the bubble radius for  $\text{N}_2$  foams in cylindrical geometry (●) (data from ref. 16) and in spherical geometry (\*).

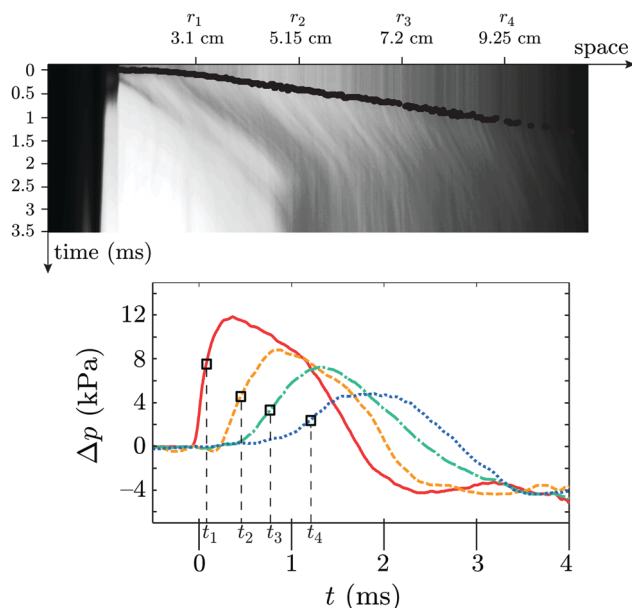


Fig. 14 (top) Spatio-temporal image of the foam. The pressure wave propagates from the left to the right. The symmetry axis coincides with  $r = 0$ , and the position of the four sensors is indicated. The wave front (black line) has been determined by image processing. (bottom) Pressure signals obtained for the same experiment plotted as a function of time. The four squares represent the arrival time  $t_i^{\text{im}}$  of the wave front at each sensor position, as determined on the spatio-temporal image above.

both behaviours appears sharply on the diagram and corresponds to the front wave arrival time. It has been determined by image processing and is represented by the black line on the diagram. The slope of this line is the front wave velocity. The times  $t_i^{\text{im}}$  are defined as the times corresponding to the positions of the four sensors on this line. They have been reported on the pressure signals in Fig. 14 (bottom). At each sensor, the time  $t_i^{\text{im}}$  roughly coincides to  $t_{1/2,i}$ , defined as the time for which the pressure reaches half its maximal value at sensor  $i$ . This justifies that the velocity deduced from the image and  $t_i^{\text{im}}$  represents the same physical quantity as the velocity deduced from the pressure signal and  $t_{1/2,i}$ .

## Acknowledgements

The authors thank S. Kerampran for regular and insightful discussions and J.-C. Potier and P. Chasle for technical support. The shock tube has been designed by following the advice of G. Jourdan and L. Houas. M. Monloubou gratefully acknowledges financial support from the DGA.

## References

- 1 R. Raspet and S. Griffiths, *J. Acoust. Soc. Am.*, 1983, **74**, 1757–1763.
- 2 I. I. Goldfarb, I. R. Shreiber and F. I. Vafina, *J. Acoust. Soc. Am.*, 1992, **92**, 2756–2769.
- 3 I. Goldfarb, Z. Orenbakh, I. Shreiber and F. Vafina, *Shock Waves*, 1997, **7**, 77–88.
- 4 I. Shreiber, G. Ben-Dor, A. Britan and V. Feklistov, *Shock Waves*, 2006, **15**, 199–204.
- 5 A. Britan, G. Ben-Dor, H. Shapiro, M. Liverts and I. Shreiber, *Colloids Surf., A*, 2007, **309**, 5–23.
- 6 A. Britan, M. Liverts and G. Ben-Dor, *Colloids Surf., A*, 2009, **344**, 48–55.
- 7 E. Del Prete, A. Chinnayya, L. Domergue, A. Hadjadj and J.-F. Haas, *Shock Waves*, 2013, **23**, 39–53.
- 8 A. B. Wood, *A Textbook of Sound*, MacMillan, New-York, 1930.
- 9 N. Mujica and S. Fauve, *Phys. Rev. E: Stat., Nonlinear, Soft Matter Phys.*, 2002, **66**, 021404.
- 10 J. Pierre, R.-M. Guillermic, F. Elias, W. Drenckhan and V. Leroy, *Eur. Phys. J. E: Soft Matter Biol. Phys.*, 2013, **36**, 113.
- 11 I. Ben Salem, R.-M. Guillermic, C. Sample, V. Leroy, A. Saint-Jalmes and B. Dollet, *Soft Matter*, 2013, **9**, 1194–1202.
- 12 J. Pierre, B. Dollet and V. Leroy, *Phys. Rev. Lett.*, 2014, **112**, 148307.
- 13 K. Kann, *Colloids Surf., A*, 2005, **263**, 315–319.
- 14 A. Prosperetti, *J. Acoust. Soc. Am.*, 1977, **61**, 17–27.
- 15 A. Prosperetti, *J. Fluid Mech.*, 1991, **222**, 587–616.
- 16 M. Monloubou, B. Dollet, A. Saint-Jalmes and I. Cantat, *EPL*, 2015, **112**, 34001.
- 17 [encyclopedia.airliquide.com/encyclopedia.asp](http://encyclopedia.airliquide.com/encyclopedia.asp).
- 18 A. Saint-Jalmes, M. U. Vera and D. J. Durian, *Eur. Phys. J. B*, 1999, **12**, 67–73.
- 19 S. Hilgenfeldt, S. A. Koehler and H. A. Stone, *Phys. Rev. Lett.*, 2001, **86**, 4704–4707.
- 20 I. Cantat, S. Cohen-Addad, F. Elias, F. Graner, R. Höhler, O. Pitois, F. Rouyer and A. Saint-Jalmes, *Foams. Structure and Dynamics*, Oxford University Press, Oxford, 2013.
- 21 G. Maurdev, A. Saint-Jalmes and D. Langevin, *J. Colloid Interface Sci.*, 2006, **300**, 735–743.
- 22 F. G. Friedlander, *Proc. R. Soc. London, Ser. A*, 1946, **186**, 322–344.
- 23 J. M. Dewey, *Proc. R. Soc. London, Ser. A*, 1964, **279**, 366–385.
- 24 J. L. Hunt, R. A. Jones and K. A. Smith, Use of hexafluoroethane to simulate the inviscid real-gas effects on blunt entry vehicles, NASA Technical Report NASA-TN-D-7701, 1974.
- 25 V. Surov, *High Temp.*, 2000, **38**, 97–105.
- 26 N. D. Denkov, S. Tcholakova, K. Golemanov, K. P. Ananthpadmanabhan and A. Lips, *Soft Matter*, 2009, **5**, 3389–3408.
- 27 J. Pierre, B. Giraudet, P. Chasle, B. Dollet and A. Saint-Jalmes, *Phys. Rev. E: Stat., Nonlinear, Soft Matter Phys.*, 2015, **91**, 042311.
- 28 H. M. Princen, *J. Colloid Interface Sci.*, 1985, **105**, 150.